Nanoscale

PAPER

View Article Online
View Journal | View Issue

Cite this: *Nanoscale*, 2014, **6**, 10033

Tuning the electrical property *via* defect engineering of single layer MoS_2 by oxygen plasma†

Muhammad R. Islam,[ab] Narae Kang,[ab] Udai Bhanu,[ab] Hari P. Paudel,[ab] Mikhail Erementchouk,[ab] Laurene Tetard,[ab] Michael N. Leuenberger[abd] and Saiful I. Khondaker*[abc]

Received 21st April 2014
Accepted 13th June 2014

DOI: 10.1039/c4nr02142h

www.rsc.org/nanoscale

We have demonstrated that the electrical property of single-layer molybdenum disulfide (MoS_2) can be significantly tuned from the semiconducting to the insulating regime *via* controlled exposure to oxygen plasma. The mobility, on-current and resistance of single-layer MoS_2 devices were varied by up to four orders of magnitude by controlling the plasma exposure time. Raman spectroscopy, X-ray photoelectron spectroscopy and density functional theory studies suggest that the significant variation of electronic properties is caused by the creation of insulating MoO_3-rich disordered domains in the MoS_2 sheet upon oxygen plasma exposure, leading to an exponential variation of resistance and mobility as a function of plasma exposure time. The resistance variation calculated using an effective medium model is in excellent agreement with the measurements. The simple approach described here can be used for the fabrication of tunable two-dimensional nanodevices based on MoS_2 and other transition metal dichalcogenides.

Introduction

The discovery of graphene, by mechanical exfoliation from a layered bulk solid to a single atomic layer, and its extraordinary mechanical, electrical and optical properties have stimulated significant interest in other two dimensional (2D) materials and their heterostructures.[1–6] A unique aspect of 2D materials is that they can exist with various intrinsic electronic properties such as metal, semimetal, semiconductor or insulator, which is defined by their coordination chemistry.[7] Among the different 2D materials, graphene (semimetal) and molybdenum disulfide (semiconductor) have been receiving the most attention. While graphene has very high mobility, the lack of a bandgap in its electronic structure limits its application in nanoelectronics and optical devices. On the other hand, MoS_2, a member of the transition metal dichalcogenides (TMDC) family, offers a layer-dependent electronic bandgap: bulk MoS_2 is an indirect bandgap material with a gap of 1.2 eV which transitions into a direct bandgap of 1.8 eV in a single layer MoS_2.[8] As a result, field effect transistors (FETs) based on single-layer MoS_2 have shown a current switching of up to 10^8 [ref. 9]. In addition, it was shown that the mobility of the MoS_2 FETs is also layer dependent: it increases with the number of layers up to 10 layers and then decreases for higher thicknesses.[10] Consequently, single and multi-layer MoS_2 have been extensively studied and hold great promise for future applications in nano-electronic devices. In fact, several prototype devices based on single and multilayer MoS_2, such as phototransistors, chemical sensors, photovoltaic devices, diodes, memory devices and integrated circuits, have already been demonstrated.[9–19]

Electrical and optical property variations have been observed with the number of layers, however, a more recent effort has been focused on engineering the material properties of the single layer MoS_2 by an external control. The grand challenge is to determine whether the metal, semiconductor, and insulator 'phases' can be realized in the same 2D material using an external control without resorting to multiple 2D materials. Since the 2D materials are atomically thin, their electronic and optical properties are highly sensitive to the external control. For example, metallic behavior has been found in lithium intercalated single-layer MoS_2.[20] A theoretical study predicts that, owing to its lower symmetry, strain engineering can be used to tune the MoS_2 bandgap, which can in turn modulate electrical and optical properties. For example, it was predicted that a transition from a direct to an indirect bandgap can be achieved in single-layer MoS_2 by strain engineering.[21–23] Recent experiments have suggested that electronic structure

[a]Nanoscience Technology Center, University of Central Florida, Orlando, Florida 32826, USA. E-mail: saiful@ucf.edu
[b]Department of Physics, University of Central Florida, Orlando, Florida 32826, USA
[c]School of Electrical Engineering and Computer Science, University of Central Florida, Orlando, Florida 32826, USA
[d]College of Optics and Photonis (CREOL), University of Central Florida, Orlando, Florida 32826, USA

† Electronic supplementary information (ESI) available: (1) Resistance *versus* plasma time for Vg = 20 V. (2) Effect of oxygen plasma on a second single-layer device. (3) Scanning electron microscope image of a plasma-exposed MoS_2 flake. (4) Theoretical calculation of resistance. See DOI: 10.1039/c4nr02142h

Published on 17 June 2014. Downloaded by University of Montpellier on 19/01/2016 05:30:27.

This journal is © The Royal Society of Chemistry 2014

Published on 17 June 2014. Downloaded by University of Montpellier on 19/01/2016 05:30:27.

modification is indeed possible by strain engineering,[22] however experimental evidence of the electrical property tunablility using such a technique is still lacking. The ability to continuously modulate electronic properties in the same layer will enable the fabrication of nano-devices with a wide range of tunability of electronic and optical properties.

Here, we demonstrated a novel approach to continuously tune the electrical properties of a single-layer MoS_2 FET from the semiconductor to the insulator using an external control. The approach presented here is based on the controlled exposure of MoS_2 to oxygen plasma (an O_2–Ar mixture of 20 : 80) for different exposure times. We show that the mobility, on-current and resistance of a single-layer MoS_2 FET vary exponentially by up to four orders of magnitude with respect to the plasma exposure time. Raman studies conducted before and after plasma treatment show a significant decrease in the intensity of MoS_2 peaks with the creation of a new oxidation induced peak, while the X-ray photoelectron spectroscopy (XPS) study shows peaks associated with MoO_3 after the plasma exposure. We suggest that during the exposure to oxygen plasma, the energetic oxygen molecules interact with MoS_2 and create MoO_3-rich defect regions, which are insulating. The coverage of the defect regions increases with the exposure time. This result is confirmed by density functional theory (DFT) calculations. We have also used a theoretical model based on effective medium approximation to describe the resistance as a function of plasma exposure time. Our results show that the effective medium semiconductor (EMSC) made of MoS_2 including MoO_3 defect regions acts as a tunnel barrier for the injected conduction electrons, giving rise to the exponential increase in resistivity as a function of plasma exposure time, which is in excellent agreement with our experimental data. Our calculations demonstrate an increase in the tunnel barrier height of 0.06 eV for each second of the plasma exposure time. Our findings suggest a simple and efficient approach for the in-plane engineering of electrical properties of MoS_2 which can be applied to other TMDCs as well and will enable the fabrication of a wide range of tunable 2D nanodevices.

Experimental section

Device fabrication

The devices were fabricated using single layers that were mechanically exfoliated from a commercially available crystal of molybdenite (SPI Supplies Brand, Natural Molybdenite) using the adhesive tape micromechanical cleavage technique and deposited on a highly doped Si substrate capped with a thermally grown 250 nm thick SiO_2. Before MoS_2 deposition, the Si/SiO_2 wafers were cleaned using oxygen plasma followed by rinsing with acetone and isopropyl alcohol. Standard electron beam lithography (EBL) was used to pattern metal contacts on the MoS_2 flakes. First, a double-layer electron beam resist, methyl methacrylate/poly(methyl methacrylate) (MMA/PMMA), was spun on the substrate and baked, followed by the e-beam exposure and development in (1 : 3) methyl isobutyl ketone : isopropyl alcohol (MIBK : IPA). After defining the electrodes, 35 nm Au was deposited by thermal evaporation, followed by lift-off in acetone.

Electrical transport measurements

The electron transport measurements of the MoS_2 device were performed on a probe station at ambient conditions using a Keithley 2400 source meter and a DL instruments 1211 current preamplifier interfaced with LabView program. The measurements were performed for the pristine flake and after each oxygen plasma treatment. The plasma treatment on the MoS_2 devices was carried out using a commercial (Plasma Etch, PE-50) plasma chamber at a power of 100 W operating at 50 kHz. During plasma exposure, the pressure within the plasma chamber was held at 250–350 mTorr and a gas mixture of oxygen (20%) and argon (80%) was passed at a constant rate of 15 sccm. For the first exposure, the samples were exposed for 2 s, and subsequently they were exposed at 1 s intervals and the electron transport measurements were repeated.

Characterization

XPS was performed to analyze any possible change in the chemical composition of MoS_2 flakes due to plasma treatment on a Physical Electronics 5400 ESCA system utilizing a monochromatized Al Kα X-ray source. MoS_2 flakes containing both single layer and multi-layer were exfoliated on a SiO_2 substrate and XPS was carried out both before and after the plasma exposure. Raman spectra of the as-exfoliated and plasma-treated MoS_2 flakes were recorded with a Witec alpha300RA confocal Raman system. The MoS_2 flakes were illuminated with 532 nm laser light in the ambient air environment at room temperature. The power of the laser line was kept below 1 mW in order to avoid any damage to the flake, while maintaining a good signal to noise ratio.

Theoretical calculations

Density functional theory calculations (DFT) were performed to investigate the stability of MoOS and MoO_3 defects inside a single layer of MoS_2. For that, we performed DFT calculations for a single layer of MoS_2, a single layer of MoO_3, a single layer of MoS_2 with MoOS defects and a single layer of MoS_2 with MoO_3 defects. In each of these cases we considered a mesh of $9 \times 9 \times 1$ k-points in the Brillouin zone. The ion-electron interaction is described by the projected augmented wave (PAW) method and the exchange-correlation energy is calculated using the Perdew–Burke–Ernzerhof (PBE) approximation within the framework of the generalized gradient approximation (GGA). The grid point cutoff of 415 eV is used, and a maximum force of 0.1 eV Å^{-1} on each atom is reached during the optimization process in all cases.

Results and discussion

Fig. 1(a) shows an optical micrograph and Fig. 1(b) shows an atomic force microscopy (AFM) topographic image of a representative single-layer flake on a Si/SiO_2 substrate. The height profile of a flake shown in Fig. 1(b) indicates a thickness of

 This journal is © The Royal Society of Chemistry 2014

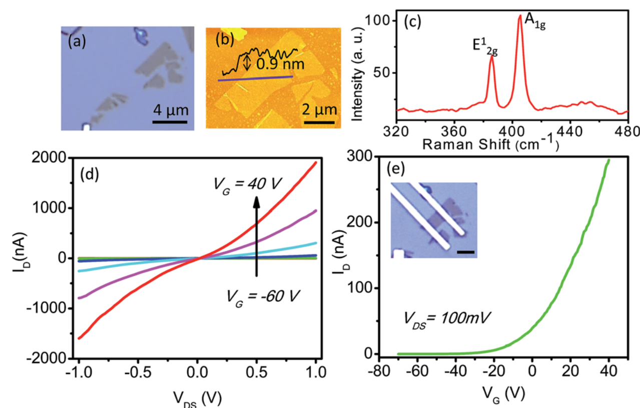

Fig. 1 (a) Optical micrograph of a single-layer MoS_2 flake exfoliated on a Si/SiO_2 substrate. (b) AFM image with a height profile. The line indicates the location of the height profile. (c) Raman spectrum of the single-layer MoS_2. (d) Output characteristics of the single-layer MoS_2 device at different back gate voltages (V_G) ranging from −60 V to 40 V with an interval of 20 V. (e) Transfer characteristics of the same device. The inset shows the optical micrograph of the device (scale bar is 2 µm).

0.9 nm, corresponding to a single layer.[17,24] The number of MoS_2 layers was further confirmed by Raman spectroscopy perfomed before making electrical contacts to the flake, as shown in Fig. 1(c). Two prominent peaks at E_{2g}^1 and A_{1g} corresponding to in-plane and out-of-plane vibrations of Mo and S atoms were separated by a Raman position difference Δ = 19.28 cm^{-1}, confirming the single layer nature of the flake.[25] Standard electron beam lithography (EBL) was used to pattern Au contacts on the MoS_2 flakes. An optical micrograph of a representative fabricated device is shown in the inset of Fig. 1(e).

Fig. 1(d) shows the output characteristics (I_D *vs.* V_{DS}) for different back-gate voltages (V_G) varying from −60 to 40 V (bottom to top) with a step of 10 V. The increase of drain current with the gate voltage indicates n-type FET behavior. The asymmetric behavior (a higher current at positive bias) suggests that a small Schottky barrier is present at the contact. Fig. 1(e) shows the transfer characteristics (drain–current I_D as a function of back-gate voltage V_G) measured at a fixed source–drain bias voltage V_{DS} = 100 mV for the pristine MoS_2 device. The I_D increased by several orders of magnitude with the increase of V_G. The current on-off ratio of the device is found to be ∼10^4. The field effect mobility of the device was calculated to be 6 cm^2 V^{-1} s^{-1} using the relation $\mu = (L/WC_GV_{DS})(dI_D/dV_G)$, where L is the channel length, W is the channel width and $C_G = \varepsilon_0\varepsilon_rA/d$ is the capacitance between the gate and SiO_2, with $\varepsilon_r \sim 3.9\varepsilon_0$ is the effective dielectric constant of SiO_2, and d (=250 nm) is the oxide thickness.[9]

Fig. 2(a) shows the transfer characteristics of the same device after different plasma exposure times. For a unified view of the curves, we multiplied the curve for the 0 s (pristine MoS_2) exposure by 0.01 and 2 s exposure by 0.5. Interestingly, the drain current at all gate voltages decreases with increasing oxygen plasma exposure. This can be more clearly seen in Fig. 2(b) (right axis) where the on-current at V_G = 40 V is displayed in a semi-log scale. The drain current was ∼285 nA for the as-fabricated sample, which decreased exponentially with time to a value of less than 20 pA, a drop of more than four orders of magnitude, after only a total of 6 s plasma exposure time. After the 6 s exposure, the current becomes negligibly small. The mobility of the device after each plasma exposure is calculated from the $I_D - V_G$ curves in Fig. 2(a), and is plotted in Fig. 2(b) (left axis) in a semi-log scale. Like the on-current, the mobility also drops exponentially from 6 cm^2 V^{-1} s^{-1} for the as-fabricated sample to 4 × 10^{-4} cm^2 V^{-1} s^{-1}, after the 6 s plasma exposure. Similar to on-current, the decrease of mobility is also more than four orders of magnitude with the plasma exposure.

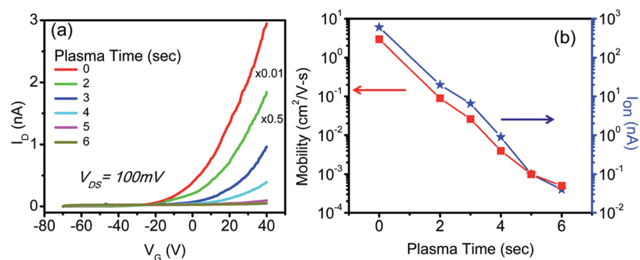

Fig. 2 (a) Gate dependence of the source drain current (I_D) after different plasma exposure times. The curve corresponds to the plasma exposure time of 0, 2, 3, 4, 5, and 6 s respectively. (b) Effect of plasma exposure on the on-current (at V_G = 40 V) and mobility of the single-layer MoS_2 device.

Fig. 3(a) shows the $I_D - V_{DS}$ graph of the device at V_G = 40 V for different plasma exposure times. It is observed that at all exposure times, the $I_D - V_{DS}$ curves are linear around the zero bias representing the Ohmic behavior, from which we can measure the resistance. Fig. 3(b) demonstrates the dependence of resistance with respect to the plasma exposure time. The resistance increased by up to five orders of magnitude with increasing plasma exposure time. The logarithmic plot in Fig. 3(b) demonstrates that the resistance increases exponentially upon plasma exposure. Similar changes in the resistance were also observed for other gate voltages (see ESI S1†). This can be described by an effective medium model which shows that the exponential increase in the resistance as a function of plasma exposure time leads to the gradual increase of the tunnel barrier raised by the effective medium semiconductor

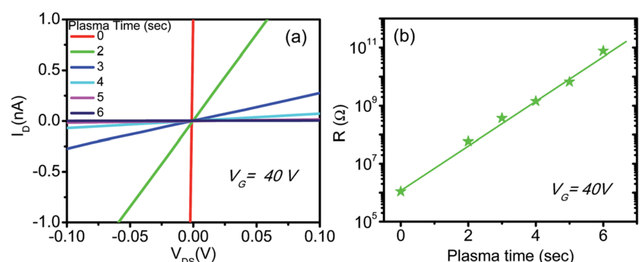

Fig. 3 (a) I_D *vs.* V_{DS} characteristics curve for the single-layer MoS_2 device after different plasma exposure times. (b) Resistance of the device as a function of plasma exposure time. The green line is the linear fit of the logarithmic resistance as a function of exposure duration.

Published on 17 June 2014. Downloaded by University of Montpellier on 19/01/2016 05:30:27.

Published on 17 June 2014. Downloaded by University of Montpellier on 19/01/2016 05:30:27.

(EMSC) material made of MoS_2 and strain-inducing MoO_3-rich defect regions.

Similar device characteristics were obtained on two other single layer devices (see ESI S2†). To explore the physical mechanism responsible for the observed change in electronic transport properties, we performed Raman spectroscopy and XPS on the pristine and plasma-treated MoS_2 flakes. Raman spectroscopy is a powerful tool to investigate changes in the composition of 2D materials. Here we compare the Raman signature of the pristine flake and the plasma-treated monolayer. Fig. 4(a) shows the Raman spectra of a representative single-layer MoS_2 flake before (red curve) and after 6 s of oxygen plasma treatment (green curve). The two Raman peaks corresponding to E_{2g}^1 (~385 cm^{-1}) and A_{1g} (~410 cm^{-1}) modes, characteristic of MoS_2 observed in the pristine flake, clearly decrease in amplitude after treatment. Interestingly, E_{2g}^1 (in plane) is severely affected as a result of the treatment, while A_{1g} shifts only by 3 cm^{-1} with strong amplitude decrease (6 times) and a significant broadening. Finally, the disappearance of LAM mode at 450 cm^{-1} also confirms the disruption of the MoS_2 lattice during the oxygen plasma treatment. On the other hand, the appearance of other peaks observed in the 150–400 cm^{-1} range, particularly at 225 cm^{-1} suggests an oxidation induced peak in the system. The XPS data presented below show the presence of a Mo^{6+} peak. Therefore, the observed oxidation induced peak in Raman data may indicate the formation of MoO_3.[26,27]

Fig. 4(b) shows the XPS spectra of pristine MoS_2 and plasma-treated MoS_2 respectively. Three prominent peaks were observed at energies 227 eV, 229.7 eV, and 233.1 eV in the pristine MoS_2 sample, the origin of which has been attributed to the binding energy of S 2s, Mo $3d_{5/2}$ and Mo $3d_{3/2}$ electrons in the Mo–S bond of the MoS_2 crystal, respectively.[28,29] All these peaks were also found at the same binding energies for the plasma-treated sample, however an additional peak at energy 236.4 eV could be observed, corresponding to the higher oxidation state Mo^{+6} (ref. 29). Although, the XPS dataset is representative of all the flakes (from single layer to >20 layers) located in the probed region (around 2 μm for the XPS beam), as the beam size is much larger than the typical single-layer MoS_2 flake size, and flakes with different thicknesses are deposited on the substrate during mechanical exfoliation, the data show the possibility of MoO_3 formation under oxygen plasma. By calculating the areas under each peak, we could obtain a rough estimate for the fraction of MoO_3 present in the sample, which in this case was ~12%.

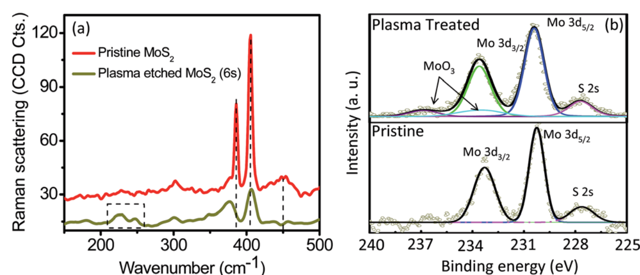

Fig. 4 (a) Raman spectra of pristine MoS_2 (red) and plasma-etched MoS_2 (green) obtained with a 532 nm excitation wavelength. The *x*-axis represents the relative shift in wavenumber (rel. cm^{-1}). While MoS_2 modes were conserved (a), new Raman peaks corresponding to the oxidation induced peak could be measured in the flake after the exposure. (b) X-ray photoelectron spectroscopy (XPS) of Mo (3d) and S (2s) core levels for pristine (lower panel) and plasma-treated (upper panel) MoS_2 flakes.

In previous experiments, oxygen and argon plasma were used on single-layer and multi-layered MoS_2 for etching purpose.[18,30,31] In order to ensure that the electrical property variation is not due to etching, we have acquired SEM images before and after the oxygen plasma treatment of a single-layer MoS_2 sample and found that the single layer was not etched after the 6 s plasma treatment (see ESI S3†). The difference with previous studies may be due to the process recipe. During the plasma process, the etching rate depends on the oxygen concentration, rf power, frequency and plasma exposure time.[32,33] The previous experiments used either a high power reactive ion etcher or a significantly longer plasma exposure time. For example, Ar plasma was recently used for thinning of multilayer MoS_2.[31] In that case, RF frequency was used and thinning was reported after 115 s of plasma exposure. In contrast, we used moderately low power and low frequency O_2–Ar plasma for a short duration (maximum 6 s). Oxygen is a strong reactive element which can change the composition of surface molecules. This suggests that the changes in the electron transport property observed in the single-layer MoS_2 are due to oxygen plasma treatment and Mo–O based defect formation.

Based on the Raman and XPS studies, we propose the following qualitative picture to explain the electrical property evolution of MoS_2: during plasma treatment high energy charged particles bombard the MoS_2 surface. Since S atoms have a smaller mass compared to Mo, S atoms can move out of the lattice site and lattice vacancies are created. Because of the excess oxygen supplied by the plasma, oxidation takes place at the defect sites created by S vacancies on the surface.[34,35] The oxidation process described as $2MoS_2 + 7O_2 \rightarrow 2MoO_3 + 4SO_2$.[27] MoO_3 has an experimentally measured bandgap of 3.2–3.8 eV, making it insulating in nature.[36] Therefore, the generation of MoO_3 in MoS_2 creates significant distortion of lattice (Fig. 5), which increases with increasing plasma exposure time. The resulting material can be treated as an EMSC which can explain the exponential variation of resistance (discussed later). The effect of MoO_3 defect regions on the transport properties of MoS_2 can be further studied at low temperature which will provide some important insights about the defect density, domain size, variable range hopping and localization lengths as has been done for 2D chemically-modified graphene.[37–40]

In the following we present our calculations based on density functional theory (DFT) as implemented in the atomistix tool kit (ATK) program (see Materials and methods). The most important fact that needs to be remembered is that a single layer of MoS_2 and a single layer of MoO_3 have completely different lattice structures. A 2D layer of MoS_2 has Mo atoms sandwiched between the S atoms with a honeycomb lattice structure as

 This journal is © The Royal Society of Chemistry 2014

Published on 17 June 2014. Downloaded by University of Montpellier on 19/01/2016 05:30:27.

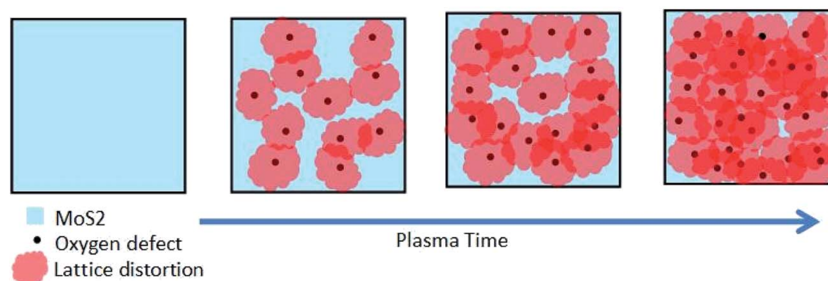

Fig. 5 Structural model of electrical property tuning *via* defect engineering in MoS_2 single-layer as a function of oxygen plasma exposure time. With the increase of the plasma exposure time, insulating MoO_3 domains are formed in MoS_2. The MoO_3-rich defect regions not only change the atomic sites locally, where they replace the S atoms, but also lead to lattice distortions. With increasing plasma exposure, the distortion also increases.

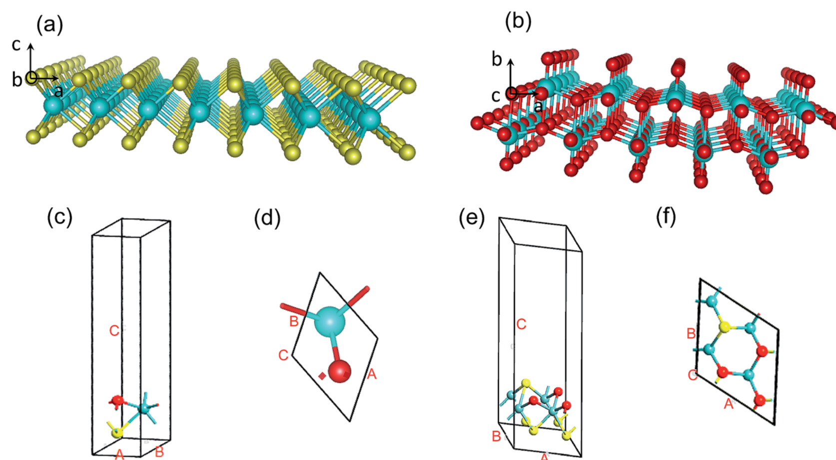

Fig. 6 A single sheet of (a) MoS_2 and (b) MoO_3. Such sheets are weakly attached by the van der Waals bond along the [001] direction in MoS_2 and [010] direction in MoO_3. (c) Top and (d) side view of the optimized structure of MoS_2 with a single O atom (red) replaced by a single S atom (yellow) in the unit cell. (e) Top and (f) side view of the optimized structure of MoS_2 with three S atoms replaced by three O atoms in a 2 × 2 supercell, where it is evident that the covalent bonds form between one of the molybdenum atoms (cyan) and the three O atoms, providing evidence for the stable configuration containing a MoO_3 defect.

shown in Fig. 6(a). Two (0001) MoS_2 layers bind weakly through van der Waals interaction, thus making mechanical exfoliation along the *c* direction possible. On the other hand, MoO_3 has an orthorhombic layered structure with separate layers stacked along the *b* direction. A single sheet of MoO_3 consists of bilayers with both sides terminated with O atoms, as shown in Fig. 6(b). The interlayer is bridged by the O atoms along the [100] direction. Due to the O atom termination of the single sheet of MoO_3 on both sides, there is a weak van der Waals bond that connects two sheets, as in the case of MoS_2, but along the [010] direction. Thus, the introduction of MoO_3 defects in a single layer of MoS_2 results in significant lattice distortions. Our results show that MoO_3-rich defect regions can be created by introducing oxygen and that MoO_3 defects are stable inside MoS_2 (Fig. 6), which is in line with the identification of Mo^{+6} in the XPS data and oxygen induced peak in the Raman spectra in Fig. 4. Fig. 6(c)–(f) show the change in the lattice structures in a MoS_2 2D sheet when few oxygen O (red) atoms replace the covalently bonded S (yellow) atoms. First, we replace one S atom by an O atom in the 2D unit cell and optimize the structure (Fig. 6(c)). We find that the original plane of MoS_2 is distorted and the O atom is shifted by a distance of 0.32 Å along the *c* direction after optimization (Fig. 6(c)). In addition, the O atom covalently bonds with the Mo (grey) atom by forming molybdenum oxysulphide (MoOS). We then replace three S atoms with three O atoms within a 2 × 2 supercell (doubling the lattice constant of the unit cell along the *a* and *b* directions). Fig. 6(e) and (f) show the configuration from the side view and top view, respectively. As O atoms form bonds with the Mo atom, the original plane of the S atoms is distorted. After optimization, it is evident that covalent bonds form between one of the Mo atoms and the three O atoms, providing evidence for the stable configuration containing a MoO_3 defect. Our results clearly show that when O atoms interact with MoS_2, MoO_3 defect regions form and create structural distortions of the lattice in all directions.

We also looked at the possibility of MoO_2 formation by optimizing the structure where two S atoms are replaced by two O atoms. DFT calculations show that MoO_2 defects can also exist. We note that, in the DFT calculations, we did not consider the effects of parameters such as temperature and kinetic

This journal is © The Royal Society of Chemistry 2014

Published on 17 June 2014. Downloaded by University of Montpellier on 19/01/2016 05:30:27.

energy of plasma, which may affect the outcome. However, due to the following reasons, we believe that MoO_2 may not be present in our experimental measurements: in XPS, the MoO_2 peak (MO^{+4}) occurs at the binding energy of 229.2 eV, which overlaps with the $3d_{5/2}$ peak of MoS_2 (229 eV). In addition, the O1s peak for MoO_2 overlaps with the MoO_3 peaks (MoO_2 is at 530.4 eV and MoO_3 at 530.6 eV).[41] Therefore, it is difficult to identify MoO_2 in the presence of MoS_2 and MoO_3 using the Mo(3d) spectra. In any case, our electronic transport data present clear clues that MoO_2 may not be present in our sample. The presence of any MoO_2 defects inside MoS_2 would not increase the resistance exponentially because MoO_2 is not an insulator, but a metal.[42,43] However, our transport measurements show (see Fig. 2a and 3b) that there is an exponential increase in the resistance as a function of plasma exposure time. This indicates that the transport properties of our plasma-treated MoS_2 are mainly dominated by the MoO_3 defects which block the current flow as it has a higher bandgap than MoS_2 as discussed in our EMSC theory below. Therefore, we conclude that majority of the defects in a MoS_2 sheet are MoO_3. Further study such as an intensive computational calculation on molecular dynamics or real time simulation is required to rule out theoretically the possibility of the formation of MoO_2 defects.

The XPS and DFT analysis show evidence of the presence of MoO_3 defects along with their surrounding lattice distortions due to oxygen plasma. It is clear that the effect of the plasma treatment on the structure of the MoS_2 layer is not homogeneous, as it forms regions with variable concentrations of MoO_3 defect regions in MoS_2 and a complex network of heterojunctions that affect the electron transport (Fig. 6). For a qualitative description of the effect of such a complex network on resistance, we adopt the approximation of an effective medium, which regards the plasma-treated material as an EMSC (see ESI Fig. S4†). For simplicity, we assume the EMSC has a homogeneous structure whose work function depends on the plasma exposure time (τ). Thus, we effectively have a heterostructure of EMSC – MoS_2. The electron transport through the EMSC – MoS_2 interface is determined by the respective band bending and the built-in potential $\Delta\phi(\tau)$, which depend on the concentration of defects and, therefore, depend on the plasma exposure time. It is natural to assume that with an increasing concentration of defects the built-in potential evolves towards its limiting value characterizing the MoS_2–MoO_3 interface ($\tau \to \infty$). Thus the maximal value of $\Delta\phi$ can be estimated using Anderson's rule:

$$\Delta\phi_{\max} = \phi_{MoO_3} - \phi_{MoS_2} \approx 2\text{ eV}, \quad (1)$$

where $\phi_{MoS_2} \approx 4.9$ eV (ref. 44) and $\phi_{MoO_3} \approx 6.9$ eV (ref. 45) are the respective work functions. The values of ϕ_{MoS_2} and ϕ_{MoO_3} reported in the literature vary noticeably, but in any case $\Delta\phi_{\max} > 1$ eV can be expected. Such a strong built-in potential results in a great increase of resistance $R_{\max}/R(0) \sim \exp(\Delta\phi_{\max}/k_B T) \sim 10^{12}$, where k_B is the Boltzmann constant and T is the temperature (see ESI† for details). This is well above the value of $\sim 10^4$ measured in the experiment and suggests that our final EMSC is not a crystalline MoO_3 sheet, in agreement with physical characterization. Rather, our experiment suggests that $\Delta\phi$ varies with the plasma exposure time and should have values: $0 \le \Delta\phi(\tau) \ll \Delta\phi_{\max}$. Taking this circumstance into account we can expand $\Delta\phi(\tau)$ in series with respect to τ, and keeping only the linear term we present $\Delta\phi(\tau) = \alpha\tau$, where α is the rate at which the barrier increases. Thus we obtain

$$\ln(R(\tau)/R(0)) \sim \frac{\alpha\tau}{k_B T} \quad (2)$$

for the dependence of resistance on the plasma exposure time. It is interesting to note that the results obtained from this rather simple model are in excellent agreement with our experimental results shown in Fig. 3(b), with $\alpha \approx 6 \times 10^{-2}$ eV s^{-1}. This calculation also suggests that with longer oxygen plasma exposure, the work function of the exposed region increases. For the same reason, the mobility and on-current decrease with the plasma exposure time.

Conclusions

In conclusion, we report the electrical property tunability of single-layer MoS_2 devices upon controlled exposure to oxygen plasma. The on-current, mobility and resistance can be tuned by up to four orders of magnitude by varying the plasma exposure time. Based on our Raman spectroscopy, XPS, and DFT studies, we present strong evidence that the significant decrease of mobility and on-conductance is caused by the creation of insulating MoO_3-rich disordered domains, which cause significant lattice distortions in the MoS_2 sheet upon oxygen plasma exposure. Using a simple and effective medium model we show that the tunnel barrier of the plasma-treated MoS_2 increases at a rate of $\alpha \approx 6 \times 10^{-2}$ eV s^{-1} with the plasma exposure time. The method for the electrical property tuning of MoS_2 devices described here can serve as an enabling technology for fabricating tunable 2D nanodevices for electronic and optoelectronic applications.

Acknowledgements

M.N.L. acknowledges the support from NSF (grants ECCS-0901784 and, ECCS-1128597) and AFOSR (grant FA9550-09-1-0450)).

References

1 A. K. Geim and I. V. Grigorieva, *Nature*, 2013, **499**, 419–425.
2 M. S. Xu, T. Liang, M. M. Shi and H. Z. Chen, *Chem. Rev.*, 2013, **113**, 3766–3798.
3 Q. H. Wang, K. Kalantar-Zadeh, A. Kis, J. N. Coleman and M. S. Strano, *Nat. Nanotechnol.*, 2012, **7**(11), 699–712.
4 S. Z. Butler, S. M. Hollen, L. Cao, Y. Cui, J. Gupta, H. R. Gutierrez, T. F. Heinz, S. S. Hong, J. Huang, A. F. Ismach, E. Johnston-Halperin, M. Kuno, V. V. Plashnitsa, R. D. Robinson, R. S. Ruoff, S. Salahuddin, J. Shan, L. Shi, M. G. Spencer, M. Terrones, W. Windl and J. E. Goldberger, *ACS Nano*, 2013, **7**, 2898–2926.

 This journal is © The Royal Society of Chemistry 2014

Published on 17 June 2014. Downloaded by University of Montpellier on 19/01/2016 05:30:27.

5 V. Nicolosi, M. Chhowalla, M. G. Kanatzidis, M. S. Strano and J. N. Coleman, *Science*, 2013, **340**, 1226419.
6 D. Jariwala, V. K. Sangwan, L. J. Lauhon, T. J. Marks and M. C. Hersam, *ACS Nano*, 2014, **8**, 1102–1120.
7 M. Chhowalla, H. S. Shin, G. Eda, L.-J. Li, K. P. Loh and H. Zhang, *Nat. Chem.*, 2013, **5**, 263–275.
8 K. F. Mak, C. Lee, J. Hone, J. Shan and T. F. Heinz, *Phys. Rev. Lett.*, 2010, **105**, 136805.
9 B. Radisavljevic, A. Radenovic, J. Brivio, V. Giacometti and A. Kis, *Nat. Nanotechnol.*, 2011, **6**, 147–150.
10 S. Das, H. Y. Chen, A. V. Penumatcha and J. Appenzeller, *Nano Lett.*, 2013, **13**, 100–105.
11 Z. Y. Yin, H. Li, L. Jiang, Y. M. Shi, Y. H. Sun, G. Lu, Q. Zhang, X. D. Chen and H. Zhang, *ACS Nano*, 2012, **6**, 74–80.
12 W. Zhang, C. Chuu, J. Huang, C. Chen, M. Tsai, Y. Chang, C. Liang, Y. Chen, Y. Chueh, J. He, M. Chou and L. Li, *Sci. Rep.*, 2014, **4**, 3826.
13 F. K. Perkins, A. L. Friedman, E. Cobas, P. M. Campbell, G. G. Jernigan and B. T. Jonker, *Nano Lett.*, 2013, **13**, 668–673.
14 D. J. Late, Y. K. Huang, B. Liu, J. Acharya, S. N. Shirodkar, J. J. Luo, A. M. Yan, D. Charles, U. V. Waghmare, V. P. Dravid and C. N. R. Rao, *ACS Nano*, 2013, **7**, 4879–4891.
15 M. Fontana, T. Deppe, A. K. Boyd, M. Rinzan, A. Y. Liu, M. Paranjape and P. Barbara, *Sci. Rep.*, 2013, **3**, 1634.
16 B. Radisavljevic, M. B. Whitwick and A. Kis, *ACS Nano*, 2011, **5**, 9934–9938.
17 H. Wang, L. Yu, Y. H. Lee, Y. M. Shi, A. Hsu, M. L. Chin, L. J. Li, M. Dubey, J. Kong and T. Palacios, *Nano Lett.*, 2012, **12**, 4674–4680.
18 M. K. Chen, H. Nam, S. J. Wi, L. Ji, X. Ren, L. F. Bian, S. L. Lu and X. G. Liang, *Appl. Phys. Lett.*, 2013, **103**, 142110.
19 M. K. Chen, H. Nam, S. Wi, G. Priessnitz, I. M. Gunawan and X. G. Liang, *ACS Nano*, 2014, **8**, 4023–4032.
20 G. Eda, T. Fujita, H. Yamaguchi, D. Voiry, M. Chen and M. Chhowalla, *ACS Nano*, 2012, **6**, 7311–7317.
21 P. Johari and V. B. Shenoy, *ACS Nano*, 2012, **6**, 5449–5456.
22 K. He, C. Poole, K. F. Mak and J. Shan, *Nano Lett.*, 2013, **13**, 2931–2936.
23 A. Castellanos-Gomez, R. Roldan, E. Cappelluti, M. Buscema, F. Guinea, H. S. J. van der Zant and G. A. Steele, *Nano Lett.*, 2013, **13**, 5361–5366.
24 M. Buscema, M. Barkelid, V. Zwiller, H. S. J. van der Zant, G. A. Steele and A. Castellanos-Gomez, *Nano Lett.*, 2013, **13**, 358–363.
25 C. Lee, H. Yan, L. E. Brus, T. F. Heinz, J. Hone and S. Ryu, *ACS Nano*, 2010, **4**, 2695–2700.
26 M. A. Py, P. E. Schmid and J. T. Vallin, *Nuovo Cimento Soc. Ital. Fis., B*, 1977, **38**, 271–279.
27 B. C. Windom, W. G. Sawyer and D. W. Hahn, *Tribol. Lett.*, 2011, **42**, 301–310.
28 P. A. Spevack and N. S. McIntyre, *J. Phys. Chem.*, 1993, **97**, 11031–11036.
29 J. Yang, S. Kim, W. Choi, S. H. Park, Y. Jung, M. H. Cho and H. Kim, *ACS Appl. Mater. Interfaces*, 2012, **5**, 4739–4744.
30 B. Radisavljevic and A. Kis, *Nat. Mater.*, 2013, **12**, 815–820.
31 Y. Liu, H. Nan, X. Wu, W. Pan, W. Wang, J. Bai, W. Zhao, L. Sun, X. Wang and Z. Ni, *ACS Nano*, 2013, **7**, 4202–4209.
32 S. Manolache, M. Sarfaty and F. Denes, *Plasma Sources Sci. Technol.*, 2000, **9**, 37–44.
33 X. Lu, H. Huang, N. Nemchuk and R. S. Ruoff, *Appl. Phys. Lett.*, 1999, **75**, 193–195.
34 N. M. D. Brown, N. Cui and A. McKinley, *Appl. Surf. Sci.*, 1998, **134**, 11–21.
35 J. R. Lince and P. P. Frantz, *Tribol. Lett.*, 2000, **9**, 211–218.
36 Y. J. Lee, W. T. Nichols, D.-G. Kim and Y. Do Kim, *J. Phys. D: Appl. Phys.*, 2009, **42**, 115419.
37 G. Eda, C. Mattevi, H. Yamaguchi, H. Kim and M. Chhowalla, *J. Phys. Chem. C*, 2009, **113**, 15768–15771.
38 D. Joung, L. Zhai and S. I. Khondaker, *Phys. Rev. B: Condens. Matter Mater. Phys.*, 2011, **83**, 115323.
39 D. Joung and S. I. Khondaker, *Phys. Rev. B: Condens. Matter Mater. Phys.*, 2012, **86**, 235423.
40 D. Joung and S. I. Khondaker, *J. Phys. Chem. C*, 2013, **117**, 26776.
41 F. Werfel and E. Minni, *J. Phys. C: Solid State Phys.*, 1983, **16**, 6091–6100.
42 Y. Shi, B. Guo, S. A. Corr, Q. Shi, Y. Hu, K. R. Heier, L. Chen, R. Seshadri and G. D. Stucky, *Nano Lett.*, 2009, **9**, 4215–4220.
43 J. Xie, J. Zhang, S. Li, F. Grote, X. Zhang, H. Zhang, R. Wang, Y. Lei, B. Pan and Y. Xie, *J. Am. Chem. Soc.*, 2013, **135**, 17881–17888.
44 R. Schlaf, O. Lang, C. Pettenkofer and W. Jaegermann, *J. Appl. Phys.*, 1999, **85**, 2732–2753.
45 J. Meyer, S. Hamwi, M. Kroeger, W. Kowalsky, T. Riedl and A. Kahn, *Adv. Mater.*, 2012, **24**, 5408–5427.